The Astronomical Journal, 159:201 (12pp), 2020 May https://doi.org/10.3847/1538-3881/ab7ea8

Exoplanets in the Antarctic Sky. III. Stellar Flares Found by AST3-II (CHESPA) within the Southern CVZ of TESS

En-Si Liang[1], Hui Zhang (张辉)[1], Zhouyi Yu[1], Ming Yang[1], Ji-lin Zhou[1], Michael C. B. Ashley[2], Xiangqun Cui[3,4], Fujia Du[3,4], Jianning Fu[5], Xuefei Gong[3,4], Bozhong Gu[3,4], Lei Hu[6], Yi Hu[4,7], Peng Jiang[8], Huigen Liu[1], Jon Lawrence[9], Qiang Liu[7], Xiaoyan Li[3,4], Zhengyang Li[3,4], Bin Ma[4,7,10], Jeremy Mould[11,12], Zhaohui Shang[4,7,13], Tianrui Sun[6], Nicholas B. Suntzeff[14], Charling Tao[15,16], Qiguo Tian[8], C. G. Tinney[17], Syed A. Uddin[18], Lifan Wang[4,6,14], Songhu Wang[19], Xiaofeng Wang[16], Peng Wei[1], Duncan Wright[20], Xuefeng Wu[4,6], Robert A. Wittenmyer[20], Lingzhe Xu[3], Shihai Yang[3,4], Ce Yu[21], Xiangyan Yuan[3,4], Jessica Zheng[22], Hongyan Zhou[8], and Zhenxi Zhu[4,6]

[1] School of Astronomy and Space Science, Key Laboratory of Modern Astronomy and Astrophysics in Ministry of Education, Nanjing University, Nanjing 210023, Jiangsu, People's Republic of China; huizhang@nju.edu.cn, zhouyi.yu1991@hotmail.com, zhoujl@nju.edu.cn
[2] School of Physics, University of New South Wales, NSW 2052, Australia
[3] Nanjing Institute of Astronomical Optics and Technology, Nanjing 210042, People's Republic of China
[4] Chinese Center for Antarctic Astronomy, Nanjing 210008, People's Republic of China
[5] Department of Astronomy, Beijing Normal University, Beijing, 100875, People's Republic of China
[6] Purple Mountain Observatory, Nanjing 210008, People's Republic of China
[7] National Astronomical Observatories, Chinese Academy of Sciences, Beijing 100012, People's Republic of China
[8] Polar Research Institute of China, Shanghai 200136, People's Republic of China
[9] Australian Astronomical Optics, Macquarie University, NSW 2109, Australia
[10] University of Chinese Academy of Sciences, Beijing 100049, People's Republic of China
[11] Centre for Astrophysics and Supercomputing, Swinburne University of Technology, P.O. Box 218, Mail Number H29, Hawthorn, VIC 3122, Australia
[12] ARC Centre of Excellence for All-sky Astrophysics (CAASTRO), Australia
[13] Tianjin Astrophysics Center, Tianjin Normal University, Tianjin 300387, People's Republic of China
[14] George P. and Cynthia Woods Mitchell Institute for Fundamental Physics & Astronomy, Texas A. & M. University, Department of Physics and Astronomy, 4242 TAMU, College Station, TX 77843, USA
[15] Aix Marseille Univ, CNRS/IN2P3, CPPM, Marseille, France
[16] Physics Department and Tsinghua Center for Astrophysics (THCA), Tsinghua University, Beijing, 100084, People's Republic of China
[17] Exoplanetary Science at UNSW, School of Physics, UNSW Sydney, NSW 2052, Australia
[18] The Observatories of the Carnegie Institution for Science, 813, Santa Barbara Street, Pasadena, CA 91101, USA
[19] Department of Astronomy, Yale University, New Haven, CT 06511, USA
[20] University of Southern Queensland, Computational Engineering and Science Research Centre, Toowoomba, Queensland 4350, Australia
[21] College of Intelligence and Computing, Tianjin University, Tianjin 300072, People's Republic of China
[22] Australian Astronomical Observatory, 105 Delhi Road, North Ryde, NSW 2113, Australia
Received 2019 August 1; revised 2020 February 11; accepted 2020 March 9; published 2020 April 10

Abstract

The CHinense Exoplanet Searching Program from Antarctica is a ground-based wide-field photometric survey using the AST3 and CSTAR telescopes located at Dome A, Antarctica. Blessed with the unparalleled observing conditions on the highest point of the Antarctic plateau, three remotely controlled, fully automatic telescopes (AST3-I, AST3-II, and CSTAR-II) carried out continuous high-precision photometric surveys through the polar nights of 2016 and 2017. During the observing seasons of 2016, a total of 26,578 light curves were obtained for stars within the area of the southern continuous viewing zone of TESS, covering an *i*-band magnitude range from 7.5 to 15. At $m_i = 10$, photometric precision reaches ~2 mmag, allowing possible discoveries of sub-Jupiter-size exoplanets. Here we report 20 stellar flares with *i*-band energies larger than 10^{34} erg detected in the 2016 data set of AST3-II, all from different sources. We model the stellar flares and calculate the durations, amplitudes, energies, and skewnesses. The flare properties and the stellar properties of their sources are presented in this work.

Unified Astronomy Thesaurus concepts: Stellar flares (1603); Photometry (1234); Astrostatistics (1882); Stellar activity (1580); Astronomy data analysis (1858); Surveys (1671)

1. Introduction

Stellar flares are unpredictable eruptive astronomical phenomena occurring in the stellar coronal region and the photosphere that emit strong radiation in a wide range of wavelengths from the radio to X-rays (Osten et al. 2005). Typically, these large eruptions last from several minutes to a few hours, with energy levels up to 10^{38} erg for some stars of the F or G type (Schaefer et al. 2000). Jackman et al. (2018) detected a flare event from a G8 star with an energy of 5.4×10^{34} erg, which is hundreds of times more energetic than the Carrington event—the largest solar flare ever detected (Carrington 1859; Tsurutani et al. 2003). Parker (1963) described stellar flares as the result of the release of magnetic energy through the reconnection of magnetic field lines. The mechanism behind stellar flares was further refined in later years by, for instance, Sweet (1969), Heyvaerts et al. (1977), and Shibata & Magara (2011), with the currently widely accepted model being electrons colliding with matter in the photosphere after acceleration along magnetic field lines (Allred et al. 2015).

Probing the differences between stellar flares from different types of stars can enable us to better understand the magnetic activities on the stellar surface and the evolution of stellar magnetic fields. Moreover, with increasing interest in finding habitable exoplanets, the life-threatening potential of extreme flare events is gaining more attention; extreme flares may emit

a lethal amount of ultraviolet radiation and cause the atmospheres of exoplanets to photoevaporate (Chadney et al. 2017; Lingam & Loeb 2017).

Since predicting the exact times of the eruptions of stellar flares on light curves is almost impossible, we rely on serendipitous detection from monitoring a large number of stars over long periods of time. Stellar flares are therefore a valuable byproduct from wide-field, continuous photometric surveys such as those used for finding transiting exoplanets. The Kepler spacecraft (Borucki et al. 2010) and the TESS spacecraft (Ricker et al. 2014), both designed for detecting transiting exoplanets by observing changes in stellar luminosity, have greatly enlarged the flare sample and advanced our understanding of stellar flares (Maehara et al. 2012; Balona 2012; Van Doorsselaere et al. 2017; Günther et al. 2020). Their discoveries include the detections of superflares on solar-like stars and flares on stars previously thought to be magnetically inactive, and extremely large stellar flares on late-type stars, indicating that more work is needed to understand the mechanism of stellar flares and stellar magnetic activities. Continuous observations using ground-based telescopes can be achieved either with longitude-distributed observing programs such as the Hungarian-made Automated Telescope Network (HATNet; Bakos et al. 2004) and Hungarian-made Automated Telescope Network-South (HATSouth; Bakos et al. 2013), or from observatories on the Antarctic plateau, where the polar nights are perfect for continuous astronomical observations.

The outstanding observing conditions on the Antarctic plateau were reported by Lawrence et al. (2004), where a median seeing of $0\farcs23$ was measured at Dome C. This result inspired more studies on the observing conditions at various potential sites in Antarctica. Kenyon & Storey (2006) found that the scintillation noise is reduced due to decreased high-altitude turbulence, which favors high-precision photometry. Other favorable factors include low water vapor (Shi et al. 2016), low atmospheric extinction and sky brightness (Kenyon & Storey 2006; Zou et al. 2010; Yang et al. 2017), mild wind, and superb seeing conditions starting from several meters above the ground level (Aristidi et al. 2009; Bonner et al. 2010; Fossat & Aristidi 2010; Giordano et al. 2012; Okita et al. 2013; Hu et al. 2014). After studying the observing qualities at Ridges A and B, as well as Domes A, B, C, and F through systematically comparing several important factors for astronomical observations, Saunders et al. (2009) concluded that Dome A, which is the highest point on the Antarctic plateau, has overall the best observing conditions. The superb observing qualities on the Antarctic plateau have also been proved by the results of ASTEP-South (Crouzet et al. 2010), ASTEP-400 (Daban et al. 2010; Mékarnia et al. 2016) at Dome C, the Chinese Small Telescope ARray (CSTAR; Yuan et al. 2008; Wang et al. 2011, 2012; Meng et al. 2013; Wang et al. 2014b, 2014a, 2015; Yang et al. 2015; Zong et al. 2015; Liang et al. 2016; Oelkers et al. 2016), and AST3-I (Wang et al. 2017; Ma et al. 2018) at Dome A.

To make full use of the extraordinary astronomical observing conditions of Dome A, the first two AST3 telescopes were set up at Dome A during the polar days of 2012 and 2015, respectively, making up the CHinese Exoplanet Searching Program from Antarctica (CHESPA) together with the CSTAR-II telescope. During the austral winter of 2016, more than 35,000 scientifically qualified images within the southern continuous viewing zone (CVZ) of the TESS spacecraft were obtained by the AST3-II telescope. Zhang et al. (2019a) presented the first data release of the observation data of 2016, including 26,578 light curves of different sources within the CVZ, which in turn enabled many new discoveries of periodic sources, including 221 newly found variables (Zhang et al. 2019a) and 116 new transiting exoplanet candidates (Zhang et al. 2019b). These results encouraged us to further explore the full potential of the AST3-II telescope by focusing on non-periodic signals, namely stellar flares.

The structure of the paper is as follows. We give a brief introduction of the AST3-II instrument, observation, and data reduction in Section 2. In Section 3 we describe the methods we adopted to detect stellar flares from the AST3-II data. In Section 4 we present the detected flares along with their detailed properties and in Section 5 we briefly summarize our work and discuss future prospects.

2. Instrument, Observations, and Previous Data Processing

2.1. Instrument

We refer the readers to Cui et al. (2008), Yuan et al. (2014, 2015), and Wang et al. (2017) for a more comprehensive description on the AST3 telescopes while we briefly describe the key parameters of AST3-II related to our work here. The AST3-II telescope is a modified Schmidt optical design as described in Yuan & Su (2012), with an effective aperture of 50 cm. Combined with a STA1600FT 10K×10K frame transfer CCD camera, reduced to 5K × 10K by electronic shuttering, the AST3-II telescope is able to resolve the sky with a pixel scale of 1 arcsecond, while providing a relatively large field of view of $1\fdg5 \times 2\fdg9$ in the Sloan *i*-band. When running unscheduled observations, the AST3-II telescope was remotely controlled via satellite link, while scheduled operations were fully automatic.

To withstand the harsh conditions during the polar night, the snow-proofing and defrosting hardwares were both upgraded based on the experience of the AST3-I telescope, which protected the AST3-II telescope safely through the austral winters of 2016 and 2017. The PLATO-A on-site observatory platform (Lawrence et al. 2009; Ashley et al. 2010) provided stable 1kW power, internet connectivity, and working conditions for the whole system. PLATO-A was able to operate for at least one year without maintenance. Other key parts of the system, including the telescope control computer, the hardware operation monitor, and the data storage array, were all designed by Shang et al. (2012) and Hu et al. (2016) of the National Astronomical Observatories, Chinese Academy of Science.

2.2. Observations and Previous Data Reductions

Zhang et al. (2019a) comprehensively introduced the scientific background and the strategy adopted when running the CHESPA program, which was initiated in 2012. The feasibility of the program was first proved by the six exoplanet candidates announced by Wang et al. (2014a), boosting our confidence in carrying out a long-term exoplanet searching program from Dome A. Here we briefly describe the observation mode adopted by the AST3-II telescope. Forty-eight target fields near the South Ecliptic Pole and within the southern CVZ of the TESS spacecraft were first selected. These target fields, which are all at low airmass when monitored from Dome A, would be continuously observed for 12 months by

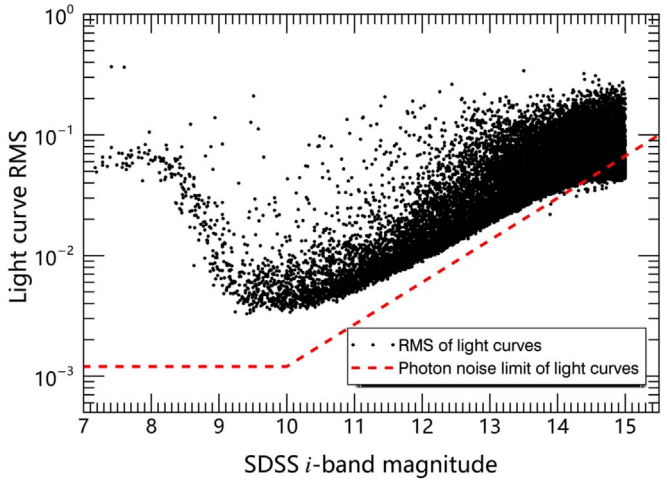

Figure 1. AST3-II photometric quality of the unclipped data from the austral winter of 2016. The y-axis, representing the light curve rms, is drawn in logarithmic scale to better illustrate the data. Black dots show the individual rms of each light curve and the red dashed line represents the photon noise limit of the light curves. At $m_i = 10$, the photometric precision reaches ~3 mmag. Note that the points combine the photometric quality and the intrinsic variability of the sources.

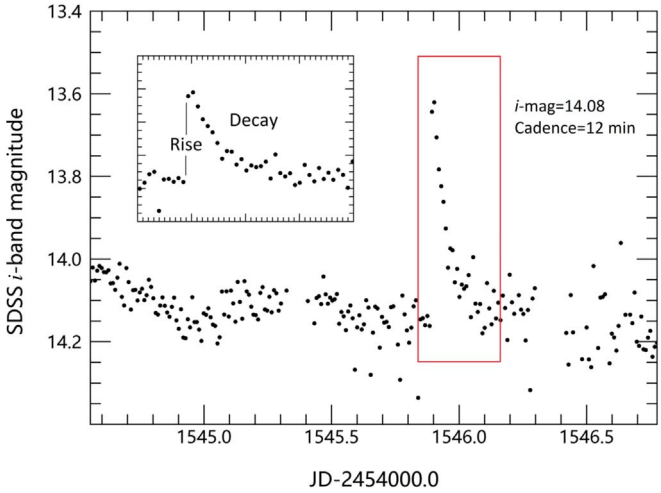

Figure 2. Telltale shape of the stellar flare event on the detrended, but not whitened, light curve of AST3II 104.3087–70.3423. Black dots are the 12 minute photometric points acquired by the AST3-II telescope and the red box marks the flare event. Data points outside the red box are considered to be the quiescent state that has relatively stable variations. The smaller panel on the upper left shows the enlarged shape of the encircled flare event, with the rise and decay phase qualitatively marked.

TESS, maximizing the collaboration between our project and the TESS project.

During the austral winter of 2016 (May 16 to June 22, the data used in this work), the first 10 target fields, with designations of AST3II004–AST3II013, were observed by the AST3-II telescope for more than 350 hr when the telescope was not in maintenance mode or making way for unscheduled events. When observing, the telescope slewed between the 10 target fields in succession to maximize the observation efficiency. Each field therefore has a 12 minute sampling cadence that includes the actual image taking time, the slewing time from one field to the next, and the CCD readout time. In order to maximize the dynamic range of the final images and avoid saturating bright stars, we adopted a three-image-stacking strategy, that is, when pointing to a target field, three images all with a 10 second exposure time were taken for later coadding.

All together, we acquired more than 35,000 scientifically qualified images in the Sloan i-band during the 2016 observation season. With a manual cutoff at the 15th magnitude, a total of 18,729 coadded images were obtained.

Aiming for millimagnitude precision for bright stars within the target fields, a customized image reduction module was described in the first paper of our series (Zhang et al. 2019a). This deals with additional systematic noises unique to our data after the standard image processing procedures, such as cross-talk and electromagnetic interference (EMI). All 26,578 aperture-photometry extracted light curves then go through the trend filtering algorithm (TFA)-based light curve detrending module to suppress the systematic trends, as described in Zhang et al. (2019b). We note that the light curves used in this work are only different from those used in the transit search in the way that the 3σ clipping step is skipped, to avoid clipping real stellar flare signals.

3. Flare Detection

3.1. Photometric Precision

As shown in Figure 1, the brightness of the stars in our work ranges from the 7th to the 15th magnitude in the Sloan i-band, with the dimmer end being a manual cutoff that is able to optimize the search efficiency. Of the 26,578 extracted sources, saturated ones are more likely to be brighter than $m_i = 10$ and show large variations. At $m_i = 10$, the best photometric precision, ~3 mmag, is reached and it worsens to ~30 mmag at $m_i = 15$. Figure 1 is slightly different from its counterparts in the first two papers of our series since the rms distribution of the light curves is slightly larger and the apparent photometric precision is not as good, due to the fact that data points outside the 3σ clipping standard are not clipped, to avoid the accidental removal of real stellar flare events.

3.2. Flare Detection Method

As mentioned in the 1, stellar flares are eruptive events with no known indicators beforehand (Jackman et al. 2018). When observed photometrically, systematically detrended light curves of stars in their quiescent state show stable small variations mostly caused by starspots on their surfaces or intrinsic pulsations. When a flare energetic enough erupts on the surface of a star, the light curve of the star shows a telltale shape that could be described as a rapid half-Gaussian rise followed by an exponential decay as shown in Figure 2 (Howard et al. 2019). These rapid rise phases show up on light curves as flux anomalies that differ from the ordinary flux difference between consecutive points in the quiescent phase, which typically follows a normal distribution.

Occasional observation interruptions, however, are unavoidable even during polar night, because of scheduled maintenance or extreme weather, resulting in common gaps on all light curves. To mitigate the negative effects of the gaps and unphysical outliers on the detection of flare events, we manually divide the light curves into 11 intervals at known common gaps larger than 10 hours and exclude data points with large photometric errors. Since stellar flares are more locally than globally prominent on light curves and have a typical duration of tens of minutes to several hours (Van Doorsselaere et al. 2017), we search for flare events in further divided

segments that have a 10 hr duration and move every three hours.

Following Liang et al. (2016), a flux anomaly is defined as a flux difference greater than $\mu_{\rm fd} + 3\sigma_{\rm fd}$, where $\mu_{\rm fd}$ is the mean of the absolute flux difference of this segment and $\sigma_{\rm fd}$ the standard deviation. Given that light curves have small variations due to starspots or intrinsic pulsations that would contaminate the quiescence, a fourth-order polynomial is first applied to whiten the segment, excluding six of the consecutive points (roughly an hour) right after the flux anomaly to reduce the negative effect the flare candidate has on the whitening procedure. We then evaluate the flux trend after the anomaly to determine whether to pass this candidate onto the validation phase. The peak point of the flare candidate, which is required to be greater than $\mu_{\rm qf} + 3\sigma_{\rm qf}$, where $\mu_{\rm qf}$ and $\sigma_{\rm qf}$ have the same definitions as above, but for the quiescent flux, is restricted to be within three points after the anomaly, based on the current understanding of the behaviors of stellar flares on light curves. Two consecutive points after the peak are all required to be greater than $\mu_{\rm qf} + \sigma_{\rm qf}$ with the first one being greater than $\mu_{\rm qf} + 2\sigma_{\rm qf}$ and on a lowering trend if this candidate is passed onto the validation phase. We note that the photometric errors of the data points are also taken into account when determining the flux trend and the flux difference between the peak point and the first point after it is required to be smaller than 50% of that between the peak point and the flux anomaly to avoid detections of candidates dominated by a single prominent point.

Among 26,578 light curves, more than 300 candidates are identified by our flare detection algorithm, and passed on for further validation. A visual inspection is first carried out to exclude candidates detected due to over-whitening, which could accidentally introduce flare-like shapes when no flare events are present. Candidates that are at the start or end of an interval where insufficient data points are present are also rejected. Sixty-two candidates are eventually chosen for further validation.

3.3. Validation Process

Even though the flare detection algorithm and visual inspection procedure excluded many unreliable candidates, ground-based observations with only one band still suffer from random bad weather and residual systematic errors that can lead to false-positive flare events. Therefore to be conservative, we further validate these candidates to rule out possible false positives.

Flare events detected on a star, in principle, should be independent cases without nearby sources displaying a similar rise and decay trend at almost the epoch. If a similar trend is found, it could be the result of contamination from nearby flaring stars (detected or undetected by our algorithm) or the other way around, or the result of a brightening of part of the target field due to random weather conditions or other possible reasons. These two causes would both lead to flare-like signals at almost the same epoch on different sources that are originally quiescent. In the first case, it is rather difficult to distinguish the real flare from the contaminated one, and in the latter case all sources are false positives. We therefore exclude all candidates where a similar trend is found in neighboring sources.

For all remaining candidates, we visually check the CCD images as the second validation step to make sure that these candidates are reliable flare events in our data set. Since the bulk of the stars observed by the AST3-II telescope are dimmer than the 12th magnitude, their CCD readout values are usually of the same order as the EMI (Zhang et al. 2019a), in which case the EMI should be treated as a contamination source for flares detected on faint stars since it exhibits a brightening effect. We therefore check the CCD images of the candidates to make sure that at the epoch of flaring, detected sources were not under the influence of EMI or other contaminating effects such as cosmic rays.

After a thorough validation process, we confirmed 20 reliable flare events in the 2016 AST3-II data set.

4. Result

4.1. Result of Flare Searching Process

In 26,578 light curves from the AST3-II 2016 data set that have Sloan *i*-band magnitudes ranging from the 7th to the 15th, we reliably confirm 20 stellar flares, all from different sources, using a robust and customized detection method. The detected stellar flares and fitted flare models are shown in Figure 3. Properties of the stellar flares, along with the properties of their sources are listed in Table 2. The light curves of the listed sources are available online.[23]

4.2. Flare Fitting Procedure

As described in Section 2.2, the sampling cadence of the transit-hunting observation mode of the AST3-II telescope on individual target fields was roughly 12 minutes. Stellar flares, however, from their time of eruption to that of total dissipation, usually occur on a timescale of tens of minutes, resulting in an under-sampling effect when searching for them in data optimized for planet hunting. Occasional interruptions in data taking causes additional discontinuity between observations, making it difficult to directly compare flare shapes from the original data points. Fitting of flares is therefore an essential part of revealing the true nature and accurately determining the properties of the detected stellar flares.

Liang et al. (2016) adopted the flare shape description function introduced by Pitkin et al. (2014), where on a light curve, before a stellar flare reaches its peak, it exhibits a rapid half-Gaussian rise, while after its peak, a slower exponential decay. In this work, we slightly modify this function to better account for the fourth-order whitened light curve by adding a constant that represents the average flux in the form of

$$F_{\rm flare} = F_{\rm av} + F_{\rm high}\begin{cases} e^{-\lambda_{\rm r}(t-T_{\rm peak})^2} & \text{if } t < T_{\rm peak} \\ e^{-\lambda_{\rm d}(t-T_{\rm peak})} & \text{if } t > T_{\rm peak}, \end{cases} \quad (1)$$

where $F_{\rm flare}$ is the observed flux, $F_{\rm av}$ is the quiescent flux after local whitening, $F_{\rm high}$ is the fitted highest point during the flare event, $T_{\rm peak}$ is the time the flare reaches its maximum, t is the time with respect to the jump point (lower one of the flux anomaly), and $\lambda_{\rm r}$ and $\lambda_{\rm d}$ are the Gaussian rise constant and the exponential decay constant, respectively.

Best-fit values of all five parameters are carried out using the Levenberg–Marquardt method. In Table 1 we list the fitted parameters of all 20 stellar flares with errors of fit included, and in Figure 4, we show the revealed peak of the flare event on AST3 J104.3087-70.3423, which also demonstrates the importance of the flare fitting procedure.

[23] http://casdc.china-vo.org/archive/ast3/II/dr1/

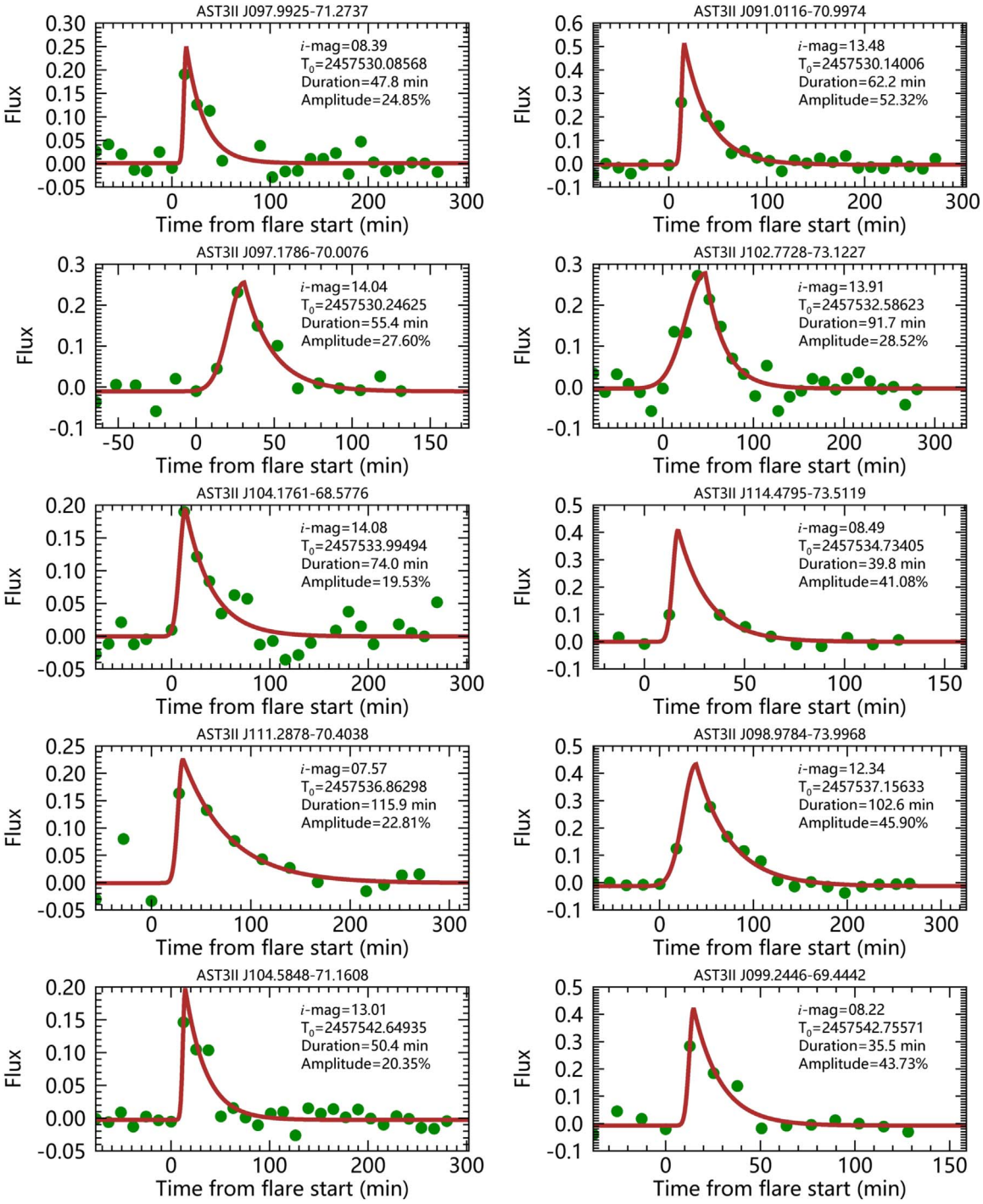

Figure 3. Twenty confirmed *i*-band flare events detected in the AST3-II 2016 data set. The designation of each flaring source is at the top of each panel. The *i*-band magnitude, starting date (in JD), duration, and amplitude of each flare event is presented on the upper right corner of each panel. Green data points are of 12 or 30 minute cadence, from the locally whitened light curves, and the fitted flare events are shown using red curves. The flare events are arranged in order of their starting dates and slightly different abscissa scales are used to best represent the shapes of each flare event.

4.3. Properties of Confirmed Flares

Stellar flares, as they appear on light curves, have several important properties that may reflect the magnetic activities on the surface of the flaring sources, including their duration, amplitude, energy, and skewness (Liang et al. 2016). By fitting the detected flares, these parameters can be better studied than using the original data points alone.

To minimize the effect of the residual flux variation after whitening on calculating the durations, we define the duration of a detected stellar flare as the time between two points on either side of the peak that are one-tenth of $F_{\rm high}$. The shortest stellar flare we detected has a duration of 28 minutes, and the longest one of 119 minutes. Figure 5 shows the histogram for the durations of all 20 detected stellar flares. As commonly accepted, stellar flares occur on a timescale between tens of minutes and several hours, with most of them concentrating under one hour. The decreasing trend shown in Figure 5 is consistent with that in Van Doorsselaere et al. (2017) which

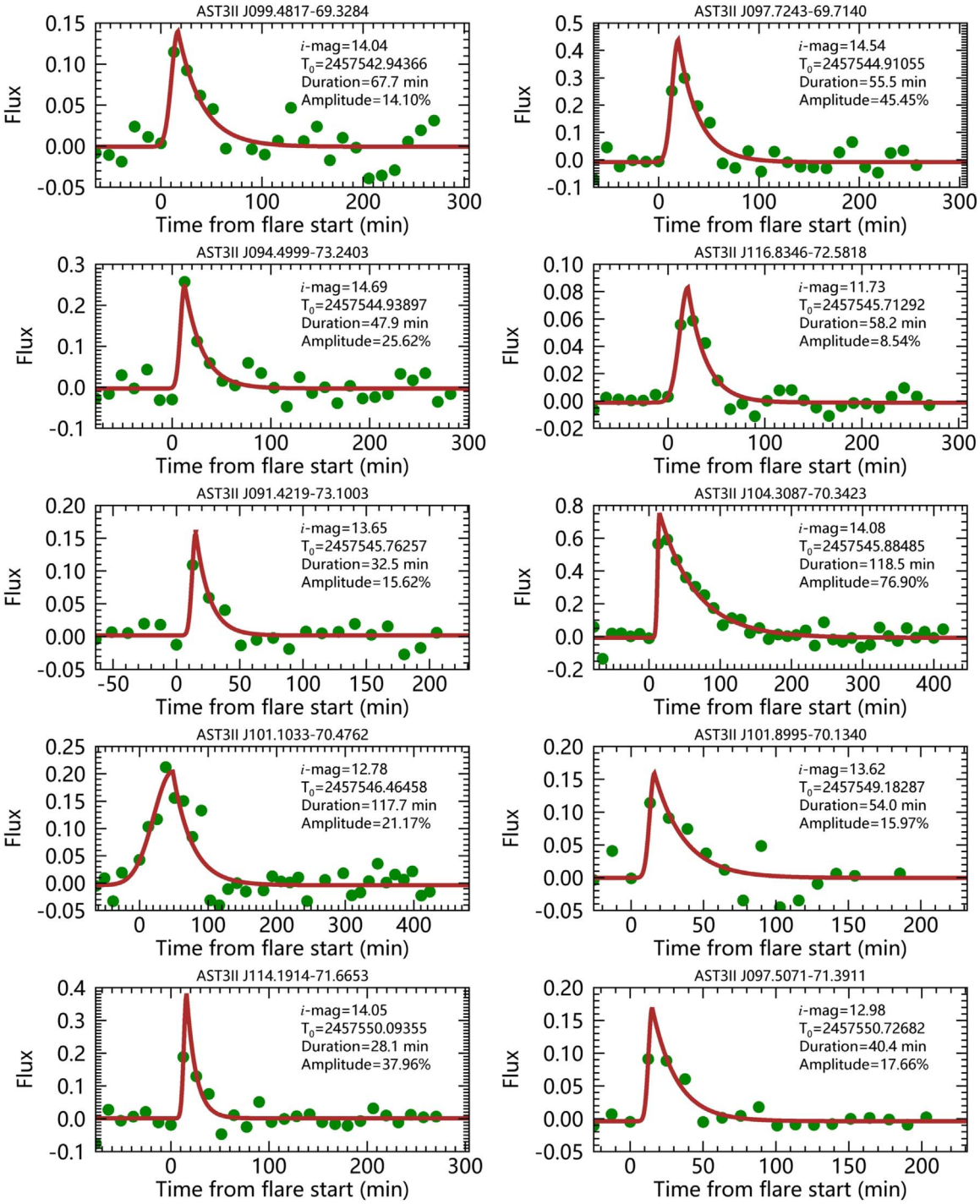

Figure 3. (Continued.)

used Kepler $Q15$ data to study the durations of stellar flares. We note that no flares under half an hour are found because our detection method requires at least four points to confirm a flare event, which corresponds to about 36 minutes.

The amplitude of each detected flare event is defined using parameters from Equation (1), which is in the form of

$$A = (F_{\rm high} - F_{\rm av}) \times 100\%, \quad (2)$$

where $F_{\rm high}$ and $F_{\rm av}$ have the same definitions as described above. Since the bulk of the observed stars are dimmer than 12th magnitude—where the photometric rms precision is larger than 1%—our 3σ standard for detecting stellar flares would result in detections with amplitudes of at least 3%. In fact, for the AST3-II 2016 data set, the smallest confirmed stellar flare has an amplitude of 8% on an F-type star with an i-band magnitude of 11.73. The amplitudes of other confirmed events range from 14% to 77%, where we note that using actual observation data points as flare peaks would greatly underestimate the true amplitudes of some of the events, indicating the importance of using a flare model when determining flare parameters.

Table 1
Fitted Parameters of All Detected Flare Events in AST3-II 2016 Data Set

AST3 ID AST3II+J	$T_{\rm peak}$ (min)	$T_{\rm peak}-$ $\times10^{-2}$	$T_{\rm peak}+$ $\times10^{-2}$	$F_{\rm av\_whitened}$ $\times10^{-3}$	$F_{\rm av\_whitened}-$ $\times10^{-3}$	$F_{\rm av\_whitened}+$ $\times10^{-3}$	$F_{\rm high}$ $\times10^{-2}$	$F_{\rm high}-$ $\times10^{-3}$	$F_{\rm high}+$ $\times10^{-3}$	$\lambda_{\rm r}$ $\times10^{-2}$	$\lambda_{\rm r}-$ $\times10^{-5}$	$\lambda_{\rm r}+$ $\times10^{-5}$	$\lambda_{\rm d}$ $\times10^{-2}$	$\lambda_{\rm d}-$ $\times10^{-5}$	$\lambda_{\rm d}+$ $\times10^{-5}$
097.9925–71.2737	14.51	−1.95	1.95	0.88	−0.59	0.56	24.94	−0.60	0.48	9.50	−252.07	258.37	5.45	−3.71	3.93
091.0116–70.9974	15.78	−17.51	328.39	−4.45	−19.21	17.97	51.88	−45.06	9.74	7.07	−5705.72	829.15	3.92	−109.69	91.95
097.1786–70.0076	30.79	−3.03	3.18	−10.42	−31.87	30.09	26.56	−3.27	3.46	0.51	−14.21	14.17	5.51	−14.31	14.06
102.7728–73.1227	46.88	−12.22	11.89	−3.65	−39.87	37.63	28.15	−4.07	4.33	0.11	−3.40	3.53	4.69	−97.45	92.94
104.1761–68.5776	14.14	−34.85	25.14	−0.42	−33.09	31.19	19.49	−6.78	6.42	1.48	−35.02	53.20	3.70	−152.99	128.01
114.4795–73.5119	16.83	−9.48	4.15	−0.32	−0.52	0.49	41.05	−1.20	2.57	7.35	−150.34	360.62	6.71	−1.04	0.98
111.2878–70.4038	31.66	−10.92	2.99	−0.79	−0.30	0.29	22.73	−0.16	0.52	2.13	−36.72	140.47	2.15	−1.04	0.98
098.9784–73.9968	38.92	−26.49	26.97	−12.86	−6.69	6.32	44.61	−3.06	3.02	0.27	−8.76	8.91	2.73	−0.05	0.04
104.5848-71.1608	14.35	−3.41	3.94	−2.67	−6.44	6.08	20.08	−1.53	1.73	9.52	−334.94	273.53	4.77	−19.37	19.78
099.2446–69.4442	14.77	−1.32	1.33	−7.27	−0.55	0.52	43.00	−0.44	0.49	9.57	−147.77	148.37	6.99	−2.48	2.34
099.4817–69.3284	16.93	−3.71	0.75	−0.58	−18.72	17.61	14.05	−2.55	2.35	1.23	−80.20	93.27	4.18	−256.75	226.00
097.7243–69.7140	19.45	−303.07	73.60	−8.54	−39.44	37.12	44.60	−19.58	77.29	1.36	−354.51	5217.17	4.94	−83.80	71.84
094.4999–73.2403	12.68	−0.00	0.00	−2.89	−43.94	41.54	25.33	−7.15	6.80	2.98	−243.65	1439.27	5.58	−223.62	210.42
116.8346–72.5818	20.62	−6.53	6.66	−1.20	−4.71	4.45	8.42	−0.28	0.28	0.69	−6.31	6.03	5.37	−77.69	79.08
091.4219–73.1003	15.25	−10.48	18.84	1.69	−22.29	21.02	15.79	−1.35	1.28	6.44	−530.93	634.42	9.17	−808.16	1138.14
104.3087-70.3423	14.68	−3.65	7.12	−7.41	−31.29	29.55	76.16	−2.59	2.01	8.33	−724.76	416.13	1.95	−8.50	8.16
101.1033–70.4762	48.59	−17.13	16.74	−3.76	−18.82	17.76	20.80	−3.54	3.26	0.06	−3.53	3.88	3.56	−0.76	0.22
101.8995–70.1340	16.05	−63.93	175.77	−0.33	−28.55	26.23	15.93	−2.83	9.49	4.66	−3588.33	2589.51	4.86	−519.52	520.03
114.1914–71.6653	16.02	−52.05	125.26	1.41	−19.60	18.32	38.10	−23.92	10.36	6.70	−2673.83	1380.04	10.54	−2149.91	2536.42
097.5071–71.3911	15.12	−4.85	3.96	−3.62	−9.41	8.88	17.30	−0.27	0.40	8.19	−241.64	324.96	5.98	−14.43	15.03

Note. Fitted parameters of all detected flare events in the AST3-II 2016 data set based on Equation (1), where $T_{\rm Peak}$ is the fitted peak time of each flare event after the jump point, $F_{\rm av}$ is the average of the fitted quiescent flux after local whitening, $F_{\rm high}$ is the fitted highest point, and $\lambda_{\rm r}$ and $\lambda_{\rm d}$ are the rise and the decay parameters of each detected flare event, respectively. The signs (−, +) following each parameter denote the lower and upper limit of each fitted parameter.

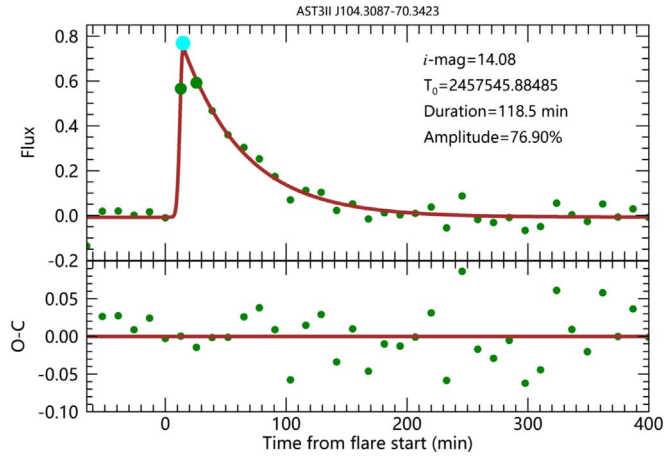

Figure 4. Fitted flare model to demonstrate the importance of fitting detected flares. Based on Equation (1), the red curve denotes the fitted flare model, and the green points are locally whitened photometric points. The relatively larger cyan point sitting at the junction at the top marks the fitted peak, which observations usually miss. The lower panel shows the difference between the original data points and the fitted model.

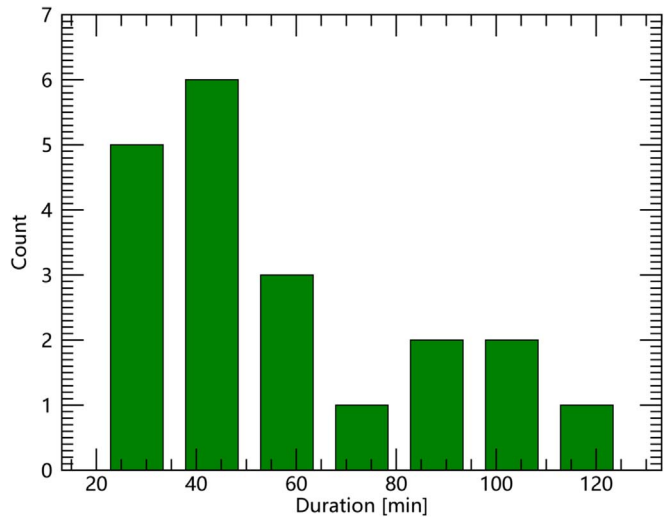

Figure 5. Histogram of the durations of detected AST3-II flares. Green bars show the number of flares in each interval, from 25 to 120 minutes, with a 20 minute bin size. Though the number of detected flares is small, a decreasing trend is apparent, where flares with longer durations are fewer, as predicted by theories.

Estimating the energies of the flare events, on the other hand, is more complicated than calculating the parameters above. As discussed in Davenport (2016) and Kowalski et al. (2013), it is known that the spectra of the energy dissipation phase during a flare has changing temperatures and non-thermal emission, making estimating the total energy of a flare event impossible using observations from only one band. We therefore take a step back and estimate only the *i*-band energy of each flare event.

We first compute the equivalent duration (ED; in units of seconds) of each flare event by integrating for the total area under the fitted flare event between its start and end as defined above. The Sloan *i*-band magnitude of each flaring source is then converted to its corresponding energy value based on Fukugita et al. (1996). Lastly, by making use of the accurate distance data from the Gaia DR2 database (Gaia Collaboration et al. 2016, 2018; Bailer-Jones et al. 2018), we calculate the *i*-band energy each flare event released.

Even though the energies of the detected stellar flares are of only one band, all of them are still larger than the largest flare event ever recorded on the surface of the Sun by two orders of magnitude, with the most energetic one releasing at least 10^{38} erg energy (AST3II J114.4795-73.5119) during one eruption, enough to cause catastrophic effects on the atmospheres of nearby planets. It is also shown in the lower left panel of Figure 6 that, on average, flare events on giant stars are more energetic than those on dwarf stars. This result is all the more interesting since on evolved stars, magnetic activities should have died down during their evolution, indicating that the flaring mechanism for giant stars could potentially be different from that of the main-sequence stars. We will discuss the determination of the luminosity class and the spectral type of the flaring sources later in this section.

Following Liang et al. (2016), we also use the skewness parameter to investigate the energy injection and dissipation phase of a flare event. The skewness parameter κ is in the form of

$$\kappa = \frac{T_{\rm des}}{T_{\rm asc}}, \tag{3}$$

where $T_{\rm asc}$ represents the time from the start of the flare to its peak, and $T_{\rm des}$ is the time from the peak to the end. The seventh column of Table 2 shows the skewness of all detected stellar flares. The upper left panel of Figure 6 shows that the skewness parameters of flares on giant stars are on average the same with those of dwarf stars, with one dwarf case reaching 22, indicating an extremely skewed flare shape. The dispersion of skewness seems large, in the middle left panel of Figure 6, however, the decay time ($T_{\rm des}$) of a flare and its corresponding duration shows the same linear relation as first pointed out by Liang et al. (2016). In this work, we improved this plot by better defining the start and end of a flare event. Using a linear fit with only the slope as the fitted parameter, we obtain a slope value of 0.75 for flares on all sources. A simple mathematical transformation then gives the corresponding average skewness as three, which is similar with that of Liang et al. (2016), indicating that the energy dissipation phase typically takes three times longer than the energy injection phase.

4.4. Stellar Properties

Aiming to better understand the detected flare events, it is necessary to collect stellar information of all flaring sources. To achieve this, we make use of the VizieR database (Ochsenbein et al. 2000) and cross-match for the same source in different catalogs in a 2″radius circle. The *BV* magnitudes are from the AAVSO Photometric All-Sky Survey (APASS) catalog (Henden et al. 2015, 2016), the *JHK* magnitudes are from the Two Micron All Sky Survey (2MASS) catalog (Skrutskie et al. 2006), and the proper motions, radii, distances, and effective temperatures of the flaring sources are all extracted from Gaia DR2 (Gaia Collaboration et al. 2016, 2018; Bailer-Jones et al. 2018).

Existing information on the spectral types and luminosity classes of the 20 flaring sources is fairly sparse. Classifying the stars, however, is important, since current understanding of the

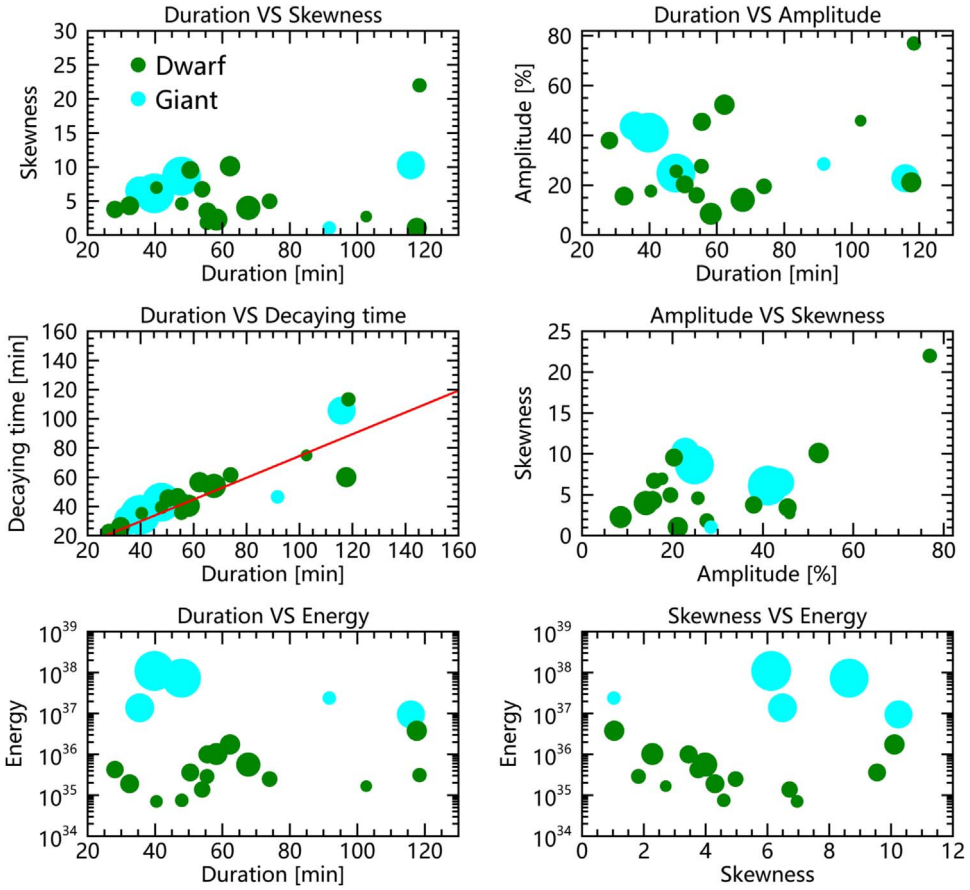

Figure 6. Statistical plots of the properties of detected stellar flares. In the order of left to right, and upper to lower, the panels show duration vs. skewness, duration vs. amplitude, duration vs. decaying time, amplitude vs. skewness, duration vs. energy, and skewness vs. energy. In all six panels, cyan points are giant stars (both known and estimated), and green points show estimated dwarf stars, with the sizes of the points logarithmically scaled to represent the stellar radii. In the middle left panel, the red line shows the linear fit of the decay time against the duration of the flares detected. We note that in the lower right panel, one source with a large skewness parameter is not shown for aesthetic reasons.

flaring mechanism requires a magnetically active star, making flaring stars thought to be magnetically weak precious cases. With the high-precision parallax data from Gaia DR2, we determine the luminosity class of each flaring source using a color–magnitude diagram (M_V versus $V-K$), as shown in Figure 7, where M_V is the absolute V-band magnitude of each flaring source calculated using the V_{mag} value and distance data listed in the tenth and twentieth column of Table 2. Two of the detected sources are known Type III giant stars that are on the upper right part of the plot where giant stars normally reside; 15 of the rest are classified as dwarf stars while the other three are giant stars. We then calculate the spectral types of the dwarf stars using the effective temperatures from Gaia DR2 and $B-V$ magnitudes from the APASS catalog based on Pecaut & Mamajek (2013). Interestingly, of all 15 dwarf flaring sources detected, the latest type is K6, not even a very late K-type dwarf, while the earliest one is of spectral type F7, a type originally to thought to be magnetically weak. We note that the radii of AST3II J102.7728-73.1227 and AST3II J099.4817-69.3284 are not available in the VizieR database; for consistency reasons, we plot these two sources with radii of $0.8R_\odot$ and $5.0R_\odot$ in Figures 6 and 7 based on their spectral types and luminosity classes.

By cross-matching with the first two works of this series, we have also found four of the flaring sources to be variables. A particular interesting case is the flaring source AST3II J097.9925–71.2737, which has a transit signal with a period and a duration of 3.4102 days and 3.838 hr, respectively. Even though the Gaia mission measures its radius to be $60.6R_\odot$, making any transiting companions more likely to be stellar objects, the TESS Input Catalog (TIC; Stassun et al. 2018) assigns it a radius of $0.18R_\odot$, making it a good candidate for a planetary host. Assuming this target to be a planet-harboring star, using the mid-transit epoch from Zhang et al. (2019b), the flare event on this source occurred only 2.02 hr after mid-transit, when the planet just moved out of transit. Though the total energy of stellar flares cannot be accurately determined without spontaneous spectral observation (Kowalski et al. 2013), larger flares have a higher chance of emitting more radiation in the EUV, FUV, and XUV bands, which are the directly responsible for the photoevaporation process in planetary atmospheres (Sanz-Forcada et al. 2011). In the case of AST3II J097.9925–71.2737, its flare with an i-band energy of 7.3×10^{37} erg, could be the indicator of enough UV radiation that is able to permanently destroy the atmosphere of that planet (Rubenstein & Schaefer 2000; Chadney et al. 2017; Lingam & Loeb 2017).

Of all the flaring dwarfs we have detected, three are F-type dwarfs, seven are G-type dwarfs, and five are K-type dwarfs. Even though flares on late-type stars (such as late K-type and M-type) are theoretically more frequent and energetic compared to their quiescent state, large rms due to low stellar

Table 2
Confirmed *i*-band Flares in AST3-II 2016 Data

AST3 ID AST3II+J	*i* (mag)	T_0 (2456000.0+)	Duration (minutes)	Amplitude %	Energy (erg)	Skewness	$B-V$ (mag)	*B* (mag)	*V* (mag)	*J* (mag)	*H* (mag)	*K* (mag)	μ_α (mas yr^{-1})	μ_δ (mas yr^{-1})	Sp. Type	Lum. Class	$T_{\rm eff}$ (K)	R_* $R_\odot$	Distance (pc)	Variability
097.9925–71.2737	08.39	1530.08568	47.8	24.8	7.3e+037	8.6	1.61	12.35	10.74	5.42	4.54	4.13	−2.83	14.70	N/A	Giant	3670.15	60.60	1154.95	TC?
091.0116–70.9974	13.48	1530.14006	62.2	52.3	1.7e+036	10.1	0.90	14.96	14.06	12.30	11.82	11.73	0.93	−2.83	K3V	Dwarf	4927.00	2.56	1131.48	0
097.1786–70.0076	14.04	1530.24625	55.4	27.6	2.9e+035	1.8	0.59	14.91	14.32	13.17	12.86	12.77	−5.39	20.89	G0V	Dwarf	5927.50	1.01	833.60	0
102.7728–73.1227	13.91	1532.58623	91.7	28.5	2.4e+037	1.0	1.08	15.63	14.55	12.62	12.01	11.94	−1.38	5.96	K3.5V	Dwarf	5046.75	0.80	5264.31	0
104.1761–68.5776	14.08	1533.99494	74.0	19.5	2.5e+035	5.0	0.77	15.26	14.49	13.11	12.78	12.71	−1.69	20.84	G8V	Dwarf	5402.67	1.16	828.93	0
114.4795–73.5119	08.49	1534.73405	39.8	41.1	1.1e+038	6.1	1.65	11.91	10.26	6.09	5.24	4.89	−6.15	8.37	N/A	Giant	3530.57	71.75	1254.54	0
111.2878–70.4038	07.57	1536.86298	115.9	22.8	9.5e+036	10.2	1.20	8.95	7.75	5.72	5.25	4.95	11.39	12.85	K3	III	4626.57	9.56	192.08	EW
098.9784-73.9968	12.34	1537.15633	102.6	45.9	1.7e+035	2.7	1.01	14.06	13.05	10.99	10.44	10.32	2.72	17.85	K3V	Dwarf	4958.50	0.58	166.73	RR
104.5848-71.1608	13.01	1542.64935	50.4	20.3	3.6e+035	9.5	0.74	14.14	13.40	12.10	11.77	11.64	−9.12	5.72	G8V	Dwarf	5427.00	1.68	737.07	0
099.2446–69.4442	08.22	1542.75571	35.5	43.7	1.4e+037	6.5	1.09	9.94	8.85	6.98	6.48	6.31	0.54	7.29	K1	III	4721.76	11.03	406.32	0
099.4817–69.3284	14.04	1542.94366	67.7	14.1	5.6e+035	4.0	0.86	15.40	14.53	12.93	12.46	12.37	−0.45	0.97	N/A	Giant	4939.54	5.00	1495.69	0
097.7243–69.7140	14.54	1544.91055	55.5	45.5	1.0e+036	3.4	0.77	15.62	14.85	13.48	13.12	13.05	3.04	19.71	G9V	Dwarf	5503.70	1.77	1546.97	0
094.4999–73.2403	14.69	1544.93897	47.9	25.6	7.5e+034	4.6	0.78	15.88	15.10	13.54	13.17	13.08	−8.11	−14.29	G9V	Dwarf	5095.00	0.80	654.69	0
116.8346–72.5818	11.73	1545.71292	58.2	8.5	1.0e+036	2.3	0.54	12.61	12.06	10.81	10.55	10.51	−0.67	3.96	F7V	Dwarf	5798.50	3.45	945.94	0
091.4219–73.1003	13.65	1545.76257	32.5	15.6	1.9e+035	4.3	0.78	14.86	14.08	12.52	12.14	12.09	1.51	8.42	G9V	Dwarf	5053.09	2.01	1000.24	0
104.3087–70.3423	14.08	1545.88485	118.5	76.9	3.1e+035	22.0	1.20	16.35	15.16	12.57	11.91	11.79	−2.24	2.15	K6V	Dwarf	4188.03	0.92	379.47	RR
101.1033–70.4762	12.78	1546.46458	117.7	21.2	3.8e+036	1.0	0.55	13.60	13.05	12.01	11.69	11.64	−0.04	10.39	F9V	Dwarf	6169.33	2.53	1280.92	0
101.8995–70.1340	13.62	1549.18287	54.0	16.0	1.4e+035	6.7	0.87	14.98	14.11	12.52	12.10	11.97	3.21	23.78	K2V	Dwarf	5039.50	1.31	652.54	0
114.1914–71.6653	14.05	1550.09355	28.1	38.0	4.2e+035	3.8	0.55	14.89	14.34	13.10	12.83	12.76	−3.62	7.08	F9V	Dwarf	5832.00	1.56	1229.56	0
097.5071–71.3911	12.98	1550.72682	40.4	17.7	7.1e+034	7.0	0.78	14.12	13.34	11.98	11.63	11.52	3.74	8.40	G9V	Dwarf	6021.44	0.70	384.02	0

Note. Flare events are sorted by the start times of each flare. The definition of each column is as follows. Column (1): designation of each flaring source in AST3-II catalog Column (2): *i*-band magnitude of each flaring source after photometric calibration. Column (3): starting date of each flare event, in Julian date. Column (4): duration of each flare event, in minutes. Column (5): amplitude of each flare event, expressed as a percentage. Column (6): *i*-band energy of each flare event, in unit of energy. Column (7): skewness of each flare event. Column (8): color index of $B-V$ from the APASS catalog. Column (9–13): *BVJHK* magnitudes of the flaring sources from the APASS catalog and the 2MASS catalog. Columns (14, 15): proper motions of each flaring source from Gaia DR2. Column (16): spectral type of each flaring source from the VizieR database (if available) and Pecaut & Mamajek (2013) based on the color index of the source. Column (17): luminosity class of each flaring source from the VizieR database (if available) and our calculation using the color–magnitude diagram. Column (18): effective temperature of each flaring source from Gaia DR2. Column (19): radius of each flaring source from Gaia DR2 (if available). Column (20): distance of each flaring source from Gaia DR2. Column (21): variability of each flaring source from the first two papers of this series, where TC? is transit candidate that needs further investigation, EW is W Ursae Majoris type eclipsing variables, and RR is variable of the RR Lyrae type.

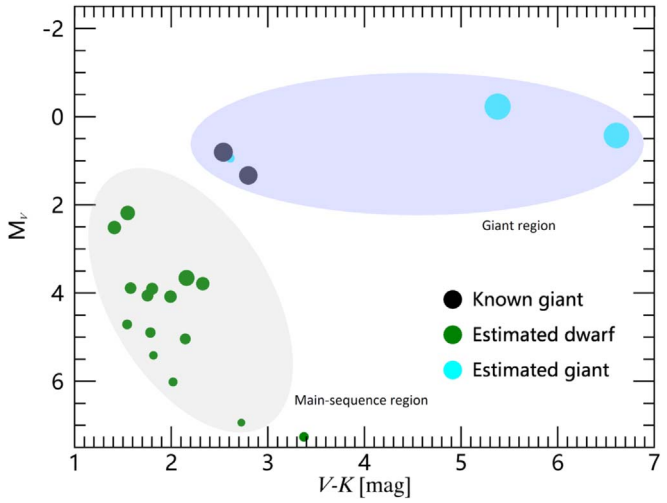

Figure 7. Simplified HR diagram of the V-band absolute magnitudes (M_V) plotted against the $V-K$ magnitudes of all flaring sources detected in the AST3-II 2016 data set. The gray and purple regions in the background are the main-sequence and giant star regions, respectively. Two black points are known giant stars from the VizieR database, while the green points and the cyan points lying in the gray region and the purple region are estimated to be dwarf and giant stars, respectively. The size of each point is based on its radius from Gaia DR2, if available, on a logarithmic scale.

luminosity makes them harder to identify or confirm especially when observed using a wide-field telescope and short cadence, which is the case this work.

5. Discussion

Located at Dome A, Antarctica, CHESPA made use of the AST3-II telescope and observed the southern CVZ of the TESS spacecraft during the polar nights of 2016 and 2017. It provided us with a valuable data set to search for transiting exoplanets, periodic variables, and transient events such as stellar flares. From 26,578 light curves we have confirmed 20 stellar flares from different sources. By fitting the flare events we provide detailed properties of the detected flares, as well as their stellar properties.

We used an improved model based on Liang et al. (2016) to fit the detected flares that can better account for whitened light curves. Limited by the sampling cadence of the AST3-II telescope and the requirement of the detection method, the durations of the detected stellar flares range from 28 minutes to 119 minutes, with most of them concentrating under 1 hr. Nineteen of 20 detected flare events have amplitudes larger than 10%, with the one on AST3II J104.3087-70.3423 being as large as 77%. We only calculated the i-band energies of the flare events, since it is impossible to constrain the whole flare spectra with data from single-band observations. Nevertheless, the energies of all detected flare events are larger than the Carrington event by at least two orders of magnitude, and energies of flares on giant stars are, on average, larger than those of dwarf stars, indicating further work is needed on the magnetic activities of evolved stars. The skewness parameter from Liang et al. (2016) is also investigated in this work. The typical ratio between the decay time and the rise time of a flare event is found to be around three.

Four of the detected flaring sources are also found to be variables, with two of them being RR Lyrae variables, one being a W Ursae Majoris eclipsing binary, and one being a transit candidate. The flare event on AST3II J097.9925–71.2737 would be energetic enough to completely wipe out the atmosphere on its tentative planet.

As the third work of the series exoplanets in the Antarctic sky, mainly focusing on stellar flares, along with the first two works that have reported discoveries of new variables and transit candidates, we have shown the power of the AST3-II telescope. After the reduction of the 2017 observation data, which is three times more than the 2016 data set, we hope our works can be useful supplement to the TESS mission.

As the second telescope of the AST3 telescope family, AST3-II has successfully proved the feasibility of utilizing the extraordinary observing conditions of Dome A during the polar night. With the successful deployment of the third AST3 telescope with a K-band camera (Burton et al. 2016), astronomical observations at Dome A will surely be fruitful in the future.

We would like to thank the anonymous referee for the very constructive and insightful comments on our original paper. We would like to express our gratitude to all the CHInese National Antarctic Research Expeditions (CHINARE) staff for installing and maintaining CSTAR, CSTAR-II, AST3-I, AST3-II, and the PLATO-A platform. We thank Nanami August for his advice on stellar flares. H.Z. is grateful to the High Performance Computing Center (HPCC) of Nanjing University for reducing the data used in this paper. E.L. is grateful for the support of Program A for Outstanding PhD candidates of Nanjing University. This research is supported by the National Basic Research Program (973 Program) of China (Nos. 2013CB834900 and 2013CB834904), the National Natural Science Foundation of China (Nos. 11933001, 11673011, 11661161014, 11333002, and 11273019), the Chinese Polar Environment Comprehensive Investigation & Assessment Program (grant No. CHINARE2016-02-03), the Australian Antarctic Division, and the Australian National Collaborative Research Infrastructure Strategy administered by Astronomy Australia Limited. X.W. is supported by the National Natural Science Foundation of China (NSFC grants 11325313, 11633002, and 11761141001), and the National Program on Key Research and Development Project (grant No. 2016YFA0400803).

ORCID iDs

Hui Zhang (张辉) https://orcid.org/0000-0003-3491-6394
Ji-lin Zhou https://orcid.org/0000-0003-1680-2940
Jianning Fu https://orcid.org/0000-0001-8241-1740
Peng Jiang https://orcid.org/0000-0002-5387-7952
Jeremy Mould https://orcid.org/0000-0003-3820-1740
C. G. Tinney https://orcid.org/0000-0002-7595-0970
Xiaofeng Wang https://orcid.org/0000-0002-7334-2357
Robert A. Wittenmyer https://orcid.org/0000-0001-9957-9304
Hongyan Zhou https://orcid.org/0000-0003-1956-9021

References

Allred, J. C., Kowalski, A. F., & Carlsson, M. 2015, ApJ, 809, 104
Aristidi, E., Fossat, E., Agabi, A., et al. 2009, A&A, 499, 955
Ashley, M. C. B., Allen, G., Bonner, C. S., et al. 2010, EAS Pub. Ser. , 40, 79
Bailer-Jones, C. A. L., Rybizki, J., Fouesneau, M., et al. 2018, AJ, 156, 58
Bakos, G., Noyes, R. W., Kovács, G., et al. 2004, PASP, 116, 266
Bakos, G. Á., Csubry, Z., Penev, K., et al. 2013, PASP, 125, 154
Balona, L. A. 2012, MNRAS, 423, 3420
Bonner, C. S., Ashley, M. C. B., Cui, X., et al. 2010, PASP, 122, 1122

Borucki, W. J., Koch, D., Basri, G., et al. 2010, Sci, 327, 977
Burton, M. G., Zheng, J., Mould, J., et al. 2016, PASA, 33, e047
Carrington, R. C. 1859, MNRAS, 20, 13
Chadney, J. M., Koskinen, T. T., Galand, M., et al. 2017, A&A, 608, A75
Crouzet, N., Guillot, T., Agabi, A., et al. 2010, A&A, 511, A36
Cui, X., Yuan, X., & Gong, X. 2008, Proc. SPIE, 7012, 70122D
Daban, J.-B., Gouvret, C., Guillot, T., et al. 2010, Proc. SPIE, 7733, 77334T
Davenport, J. R. A. 2016, ApJ, 829, 23
Fossat, E., Aristidi, E. & Astroconcordia Team 2010, EAS Pub. Ser., 40, 73
Fukugita, M., Ichikawa, T., Gunn, J. E., et al. 1996, AJ, 111, 1748
Gaia Collaboration, Brown, A. G. A., Vallenari, A., et al. 2018, A&A, 616, A1
Gaia Collaboration, Prusti, T., de Bruijne, J. H. J., et al. 2016, A&A, 595, A1
Giordano, C., Vernin, J., Chadid, M., et al. 2012, PASP, 124, 494
Günther, M. N., Zhan, Z., Seager, S., et al. 2020, AJ, 159, 60
Henden, A. A., Levine, S., Terrell, D., & Welch, D. L. 2015, AAS Meeting, 225, 336.16
Henden, A. A., Templeton, M., Terrell, D., et al. 2016, yCat, 2336, 0
Heyvaerts, J., Priest, E. R., & Rust, D. M. 1977, ApJ, 216, 123
Howard, W. S., Corbett, H., Law, N. M., et al. 2019, ApJ, 881, 9
Hu, Y., Shang, Z., Ashley, M. C. B., et al. 2014, PASP, 126, 868
Hu, Y., Shang, Z., Ma, B., & Hu, K. 2016, Proc. SPIE, 9913, 99130M
Jackman, J. A. G., Wheatley, P. J., Pugh, C. E., et al. 2018, MNRAS, 477, 4655
Kenyon, S. L., & Storey, J. W. V. 2006, PASP, 118, 489
Kowalski, A. F., Hawley, S. L., Wisniewski, J. P., et al. 2013, ApJS, 207, 15
Lawrence, J. S., Ashley, M. C., Tokovinin, A., & Travouillon, T. 2004, Natur, 431, 278
Lawrence, J. S., Ashley, M. C. B., Hengst, S., et al. 2009, RScI, 80, 064501
Liang, E.-S., Wang, S., Zhou, J.-L., et al. 2016, AJ, 152, 168
Lingam, M., & Loeb, A. 2017, ApJ, 848, 41
Ma, B., Shang, Z., Hu, Y., et al. 2018, MNRAS, 479, 111
Maehara, H., Shibayama, T., Notsu, S., et al. 2012, Natur, 485, 478
Mékarnia, D., Guillot, T., Rivet, J.-P., et al. 2016, MNRAS, 463, 45
Meng, Z., Zhou, X., Zhang, H., et al. 2013, PASP, 125, 1015
Ochsenbein, F., Bauer, P., & Marcout, J. 2000, A&AS, 143, 23
Oelkers, R. J., Macri, L. M., Wang, L., et al. 2016, AJ, 151, 166
Okita, H., Ichikawa, T., Ashley, M. C. B., et al. 2013, A&A, 554, L5
Osten, R. A., Hawley, S. L., Allred, J. C., et al. 2005, ApJ, 621, 398
Parker, E. N. 1963, ApJS, 8, 177
Pecaut, M. J., & Mamajek, E. E. 2013, ApJS, 208, 9
Pitkin, M., Williams, D., Fletcher, L., & Grant, S. D. T. 2014, MNRAS, 445, 2268
Ricker, G. R., Winn, J. N., Vanderspek, R., et al. 2014, Proc. SPIE, 9143, 914320
Rubenstein, E. P., & Schaefer, B. E. 2000, ApJ, 529, 1031
Sanz-Forcada, J., Micela, G., Ribas, I., et al. 2011, A&A, 532, A6
Saunders, W., Lawrence, J. S., Storey, J. W. V., et al. 2009, PASP, 121, 976
Schaefer, B. E., King, J. R., & Deliyannis, C. P. 2000, ApJ, 529, 1026
Shang, Z., Hu, K., Hu, Y., et al. 2012, Proc. SPIE, 8448, 844826
Shi, S.-C., Paine, S., Yao, Q.-J., et al. 2016, NatAs, 1, 0001
Shibata, K., & Magara, T. 2011, LRSP, 8, 6
Skrutskie, M. F., Cutri, R. M., Stiening, R., et al. 2006, AJ, 131, 1163
Stassun, K. G., Oelkers, R. J., Pepper, J., et al. 2018, AJ, 156, 102
Sweet, P. A. 1969, ARA&A, 7, 149
Tsurutani, B. T., Gonzalez, W. D., Lakhina, G. S., et al. 2003, JGRA, 108, 1268
Van Doorsselaere, T., Shariati, H., & Debosscher, J. 2017, ApJS, 232, 26
Wang, L., Ma, B., Li, G., et al. 2017, AJ, 153, 104
Wang, L., Macri, L. M., Krisciunas, K., et al. 2011, AJ, 142, 155
Wang, S., Zhang, H., Zhou, J.-L., et al. 2014a, ApJS, 211, 26
Wang, S., Zhang, H., Zhou, X., et al. 2015, ApJS, 218, 20
Wang, S., Zhou, X., Zhang, H., et al. 2012, PASP, 124, 1167
Wang, S.-H., Zhou, X., Zhang, H., et al. 2014b, RAA, 14, 345
Yang, M., Zhang, H., Wang, S., et al. 2015, ApJS, 217, 28
Yang, Y., Moore, A. M., Krisciunas, K., et al. 2017, AJ, 154, 6
Yuan, X., Cui, X., Gu, B., et al. 2014, Proc. SPIE, 9145, 91450F
Yuan, X., Cui, X., Liu, G., et al. 2008, Proc. SPIE, 7012, 70124G
Yuan, X., Cui, X., Wang, L., et al. 2015, IAUGA, 22, 2256923
Yuan, X., & Su, D.-q 2012, MNRAS, 424, 23
Zhang, H., Yu, Z., Liang, E., et al. 2019a, ApJS, 240, 16
Zhang, H., Yu, Z., Liang, E., et al. 2019b, ApJS, 240, 17
Zong, W., Fu, J.-N., Niu, J.-S., et al. 2015, AJ, 149, 84
Zou, H., Zhou, X., Jiang, Z., et al. 2010, AJ, 140, 602